Computation of the magnetic domain structure in bulk permalloy

Riccardo Hertel and Helmut Kronmüller
Max-Planck-Institut für Metallforschung, Postfach 80 06 65, D-70506 Stuttgart, Germany
(Received 9 March 1998; revised manuscript received 17 May 1999)

By means of three-dimensional micromagnetic finite element modeling, the Landau structure of the magnetization is calculated as a minimum energy arrangement in a rectangular permalloy block ($1\,\mu\text{m}\times 500\,\text{nm}\times 250\,\text{nm}$). On the surface, so-called Néel caps are observed. The transition between the two major domains in the prism is found to be given by an asymmetrical Bloch wall (Hubert-LaBonte wall). The result indicates an asymmetrical shape of the closure domains at the surfaces. Adaptive mesh refinement strategies are employed to raise the accuracy of the calculation. It is shown that the mesh refinement is capable to reduce discretization errors significantly. [S0163-1829(99)07733-4]

I. INTRODUCTION

After more than fifty years since the time when the basics of continuum micromagnetism have been developed by Brown[1–3] this field still poses many unsolved problems. The underlying set of coupled nonlinear equations allows analytical solutions only in the case of strong simplifications which are therefore usually an idealized model whose transferability on reality is often doubtful. In recent times, since powerful computers allow large-scale calculations it has become possible to investigate complex but nevertheless fundamental micromagnetic processes. The finite element method (FEM) has shown to be an efficient and flexible tool[4–7] for this purpose.

The first numerical calculations in this field of physics have been performed by Hubert,[8] LaBonte,[9] and Brown.[10] Since then many groups of researchers have developed programs to simulate complex magnetization processes in soft and hard magnetic materials. Although amongst the scientific community a consensus on the numerical method to be used has not yet been found and the results from different groups differ partly very strongly,[11] there is a tendency to expand the calculations on increasingly complex problems such as large-scale soft magnetic samples. Most of the calculations are usually restricted on small samples with a size that is hardly accessible for experimental investigations. Therefore, the effort to enlarge the samples on which the simulation is performed is required to bring the theoretical results into the vicinity of experimental verification or falsification in order to achieve a convincing proof of the correctness of the calculation.

Besides numerical details, there are two fundamental approaches for micromagnetic calculations. One way consists in the integration of the equation of motion of the magnetic moments described by the Gilbert equation.[12] The other method, which is used in our calculation, makes use of the fact that the equilibrium configuration of the magnetization in magnetic particles has the property to minimize the magnetic Gibbs free energy of the system.[3] A constraint that has to be observed in both methods is the preservation of the magnitude $|\mathbf{J}_s|$ of the spontaneous polarization $\mathbf{J}_s$ over the whole sample.

As the total energy consists of different competing contributions, the resulting magnetization represents a compromise between the minimization of the single components. At zero external field the total energy is the sum of the exchange energy, the magnetocrystalline anisotropy energy and the magnetostatic self-energy of the sample. To reduce the exchange energy, a homogeneous magnetization is desirable while the reduction of the stray field energy enfavors the formation of magnetic vortices. Moreover, the anisotropy energy is lowered if the magnetic moments align parallel to the easy axis. Which one of these energy terms prevails depends on the intrinsic material parameters, the geometry and the size of the sample.

II. SINGLE-DOMAIN AND MULTIDOMAIN ARRANGEMENT

If the magnetic material is sufficiently soft, i.e., $Q \ll 1$, ($Q = K/K_d$, K = magnetocrystalline anisotropy constant, $K_d = J_s^2/2\mu_0$) the effect of the anisotropy is negligible and the resulting arrangement is determined by the exchange energy and the stray field energy of the system. The result from the competition between these two energy terms mainly depends on the size of the considered sample. For a very small ferromagnetic particle the exchange term is the dominant energy contribution and a homogeneous (single-domain) arrangement is energetically favored. Increasing the size of the particle, the stray field energy of a homogeneous arrangement becomes too large as compared with the gain of exchange energy resulting from a homogeneous arrangement. Therefore, above a certain critical size of the sample the magnetization is subdivided into different domains because this subdivision of the magnetization reduces the stray field energy and simultaneously maintains the homogeneity in extended regions. The evolution from a single-domain particle to a multidomain particle with increasing size can be attributed to the scale dependence of the exchange energy density.[4] While the anisotropy energy density and the stray field energy density for a given distribution of the magnetic moments does not depend on the size of the particle, the exchange energy density is reduced with increasing size.

Analytical calculations have provided useful estimates for the critical size of hard magnetic spherical[13] particles as well as for particles of prolate spheroid shape.[14] A very coarse

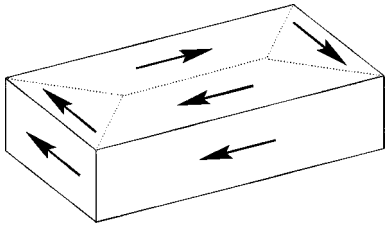

FIG. 1. Schematic illustration of the Landau structure of the magnetization in a soft magnetic rectangular block.

estimate can be derived from the simple consideration that the critical size of a sample must be at least larger than the domain wall width in order to obtain different domains in the first place. Recent computations by Rave *et al.*[15] have determined the single-domain limit of ferromagnetic cubes.

III. THE LANDAU STRUCTURE

One of the most well-defined problems in micromagnetics is the distribution of the magnetization in a rectangular soft magnetic block. Nevertheless, a detailed analysis of the magnetic structure in such a sample is still missing.

The first description of the magnetization in an iron whisker was given about sixty years ago by Landau and Lifshitz[16] who derived the four-domain pattern illustrated in Fig. 1 as an equilibrium arrangement in the case of zero external field. This pattern has been observed in several experiments, e.g., using the Bitter powder technique,[17] and according to energy considerations the formation of this structure can be understood easily: the nearly solenoidal structure of the magnetization combined with the mostly homogeneous regions is an optimal arrangement. The Landau structure represents an effective solution of the problem of the minimization of both the exchange energy and the stray field energy.

However, details in the domain walls and the effects on the surface usually have to be neglected in analytical considerations. Correspondingly, to justify this assumption, the Landau structure is usually analyzed only in the case that the typical extension of the sample exceeds the characteristic length scale of the domain wall width δ_B and δ_N significantly. A brief discussion on these length scales is given below.

IV. DOMAIN WALLS

The study on domain walls, i.e., the region between magnetic domains, is still a very active field of research. As pointed out in the textbook of Aharoni[18] and by Arrott and Templeton,[19] the calculation of the magnetization in bulk materials has not really been solved yet. However, simplified models, either analytical or numerical ones, have provided a broad knowledge about domain walls.[20]

Between the domains the magnetization changes its orientation continuously as it may not vanish due to the constraint $|\mathbf{J}_s| = \text{const}$, provided that the magnetic sample is singly connected and Feldtkeller singularities[21] are excluded. The first approach in the understanding of domain walls was given by Bloch[22] who found a continuous torsion of the magnetization around an axis perpendicular to the domain wall as a possible transition mode. The other basic model derived by Néel[23] describes the typical domain wall occurring in thin films: a rotation within the plane around an axis perpendicular to the film.

From an energetical point of view, these two wall types have strongly different attributes. A Bloch wall has a vanishing stray field energy, at least inside the bulk material. Only where the Bloch wall intersects the surface, magnetic surface charges occur. On the other hand, a Néel wall is free of surface charges but leads to volume charges ($\operatorname{div}\mathbf{m} \neq 0$, $\mathbf{m} = \mathbf{J}_s/|J_s|$ is the reduced magnetization). Therefore, it depends on the ratio of the surface to the volume of the sample which one of these wall types is energetically favored. The transition from Néel walls to Bloch walls with increasing layer thickness has been derived analytically by Néel[23] and has been shown numerically, e.g., by Ramstöck *et al.*[24] Thickness effects on the magnetic structure in elongated Permalloy particles have been investigated numerically by Koehler and Fredkin.[25] The characteristic extension of Bloch walls $\delta_B = \pi\sqrt{A/K}$ and Néel walls $\delta_N = \pi\sqrt{2\mu_0 A/J_s^2}$ (A = exchange constant) in bulk materials has been derived analytically by Kronmüller.[26] Although the extension of Néel walls depends quite strongly on the layer thickness[27] these estimates are helpful to distinguish an observed wall type as the values δ_B and δ_N may be very different.

Both the Néel wall and the Bloch wall represent strongly simplified models for the actual arrangement of the magnetization in domain walls. Generally, the most probable case for a wall transition is a mixed form of both a Néel wall and a Bloch wall.

A precise analysis of the domain walls and surfaces of the Landau pattern reveals that the structure is far more complicated than one would expect from the simple arrangement on a larger length scale. For example, the magnetization turns in plane at the surface in order to avoid magnetic poles. The Néel walls at the surface may cause a loss of symmetry which, in the simplest case, results in a magnetic vortex on one side and a 180° Néel wall on the other side of the central domain wall.[19] The Néel walls only occur as a surface effect, inside the block the transition between the domains is mostly Bloch-like. A detailed discussion on these peculiarities will be given in Sec. VII.

V. ALGORITHM

From a numerical point of view, the major problem in the accurate calculation of the Landau structure consists in the fact that on one hand one has to perform the calculation on a sufficiently large sample compared with the characteristic length scales δ_B, δ_N in order to obtain the pattern at all, on the other hand one should be able to resolve details such as wall transitions with sufficient accuracy. Only in recent times, since adaptive mesh refinement techniques for two-dimensional (2D) (Refs. 28 and 29) and especially 3D (Refs. 30 and 31) micromagnetic calculations have been developed, it has become possible to calculate the magnetization of large-scale soft magnetic particles reliably. Formerly, the examination had to be restricted on certain regions by means of idealized models. The previously mentioned calculation of the transition from Néel walls to (asymmetrical) Bloch walls,[24] e.g., was performed considering infinite strips (2D

mesh with 3D magnetic moments). With this model, finite-size effects like the formation of the closure domain structure cannot be observed. On the other hand, magnetic domain structures could hitherto only be modelled in very thin platelets ($\simeq$20–60 nm) (Refs. 32–34) because of the required discretization which cannot be achieved for bigger values of the volume of the sample. At these thicknesses Bloch walls do not occur.

In this paper we present a three-dimensional calculation of the Landau structure with an asymmetrical Bloch-wall transition between the two major domains without making use of any simplifying assumption. Even though modern computers and an improved algorithm are employed, this calculation has only been possible using adaptive meshing methods.

A. Discretization

To calculate its total energy, the system is first discretized into tetrahedral elements. This is performed using a Delaunay triangulation algorithm[35] which—in order to obtain a high number of elements with mostly uniform size—is combined with a longest-edge bisection method.[31,36]

By doing so, the volume of the sample V_0 is subdivided into N elements with the volumes V_n:

$$\sum_{n=1}^{N} V_n = V_0 . \tag{1}$$

The total energy E_{tot} of the sample is the sum of the energies of all elements,

$$E_{\mathrm{tot}} = \int_{V_0} e\,dV = \sum_{n=1}^{N} \int_{V_n} e\,dV, \tag{2}$$

where

$$e = e_{\mathrm{an}} + e_{\mathrm{ex}} + e_{\mathrm{stray}} \tag{3}$$

is the sum of the local energy densities of the anisotropy, exchange, and demagnetizing field. The task consists in the calculation of the energy $\int_{V_n} e\,dV$ of the N elements.

At each vertex i of the elements in the sample the local magnetization is defined by the polar angle ϑ and the azimuth angle φ (see Fig. 2):

$$(\mathbf{J}_s)_i = J_s \begin{pmatrix} \sin\vartheta_i \cos\varphi_i \\ \sin\vartheta_i \sin\varphi_i \\ \cos\vartheta_i \end{pmatrix}. \tag{4}$$

Using this representation, the magnetization at each node can be modified easily by an unconstrained variation of ϑ and φ. The constraint $|\mathbf{J}_s| = \mathrm{const}$ is automatically fulfilled in this way. Generally, using polar coordinates can be problematic due to the poles at the x and the z axis. For instance, the modulo 2π ambiguity of the numerical value of the polar coordinates for a given direction may cause serious problems if the angles are interpolated over an element. In order to avoid the use of subsidiary coordinate frames,[33] only the Cartesian components of the polarization are used for the calculation of each energy term. Since the Cartesian coordinates contain ϑ and φ only in terms of trigonometric expressions, the singularities of the polar coordinate systems have no effect on them.

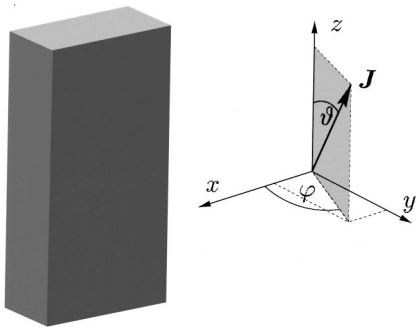

FIG. 2. The micromagnetic calculation is performed on a Permalloy block of the size 500 nm×250 nm×1 μm. The easy axis is oriented parallel to the long edge. The coordinate axes are chosen parallel to the edges: the x, y, and z axes are parallel to the medium, the short and the long edge, respectively. The origin of the coordinate frame is set at the center of the block. On the right side, the spherical coordinates ϑ and φ used to represent the local polarization are sketched.

With the data ϑ and φ for the magnetization at the vertices, the energy of an element is calculated in the most direct way by means of linear interpolation. In the following we restrict ourselves on the calculation of the energy contribution of one element. According to Eq. (2) the energy of the whole sample is straightforward.

B. Magnetocrystalline anisotropy energy

The anisotropy energy of an element

$$E_{\mathrm{an}}^{n} = \int_{V_n} e_{\mathrm{an}}\,dV = \int_{V_n} K \sin^2\alpha\,dV. \tag{5}$$

(α=angle between $\mathbf{J}_s$ and the easy axis) is calculated interpolating the energy density $e_{\mathrm{an}} = K\sin^2\alpha$ linearly over the volume of the element. For a given direction of the easy axis in the element, we have $\alpha = \alpha(\vartheta,\varphi)$. Hence, we can assign to each node i of the element the anisotropy energy density $e_{i,\mathrm{an}} = K\sin^2\alpha_i = K\sin^2\alpha(\vartheta_i,\varphi_i)$. The energy density inside the element is approximated by a spatially linear function $\tilde{e}_{\mathrm{an}}$:

$$e_{\mathrm{an}}(\mathbf{x}) \simeq \tilde{e}_{\mathrm{an}}(\mathbf{x}) = \sum_{i=1}^{4} e_{i,\mathrm{an}}\,\eta_i^n(\mathbf{x}) \tag{6}$$

using the normalized set of linear shape functions $\eta_i(\mathbf{x})$ of the element n with

$$\eta_i(\mathbf{x}_j) = \delta_{ij} \quad (i,j = 1,\ldots,4) \tag{7}$$

($\mathbf{x}_j$ is the location of the node j). By doing so, the integration of Eq. (5) can be performed easily:[37]

$$E_{\mathrm{an}}^{n} = \int_{V_n} e_{\mathrm{an}}\,dV \simeq \int_{V_n} \tilde{e}_{\mathrm{an}}\,dV = \left(\sum_{i=1}^{4} e_{i,\mathrm{an}} \right) V_n \Big/ 4. \tag{8}$$

C. Exchange energy

A different interpolation technique is required to calculate the exchange energy

$$E_{\mathrm{ex}}^{n}=\int_{V_n} e_{\mathrm{ex}}dV=\int_{V_n} A[(\nabla m_x)^2+(\nabla m_y)^2+(\nabla m_z)^2]dV. \tag{9}$$

The term e_{ex} cannot be interpolated linearly over the element as it contains spatial derivatives of the magnetization which are not defined at the vertices. Therefore we approximate the exchange energy by the assumption that the gradients $\partial m_k/\partial x_l$ with $k,l=x,y,z$ are constant within the element. Using the linear shape functions η_i^n and the well-known numerical differentiation technique of the finite element method,[37,38] the corresponding differentiations and the integral kernel in Eq. (9) are elaborated. As with this approximation the exchange energy density is spatially constant within the element, the integration in Eq. (9) becomes trivial.

D. Stray field energy

Generally, the stray field energy term

$$E_{\mathrm{stray}}=-\frac{1}{2}\int_{(\mathrm{sample})}\mathbf{H}_s\cdot\mathbf{J}_s dV=\frac{\mu_0}{2}\int_{(\mathrm{all\ space})}\mathbf{H}_s^2 dV \tag{10}$$

($\mathbf{H}_s$ = demagnetizing field) is the most cumbersome part of any micromagnetic calculation. While the first integral in Eq. (10) is over the magnetic region, the second integral is extended over all of space. The complexity of the stray field term arises from its nonlocal nature. The demagnetizing field $\mathbf{H}_s$ at the location $\mathbf{r}$ is given by

$$\mathbf{H}_s(\mathbf{r})=-\frac{1}{4\pi\mu_0}\left[\int_{V'}\frac{(\mathbf{r}-\mathbf{r}')\nabla\cdot\mathbf{J}_s(\mathbf{r}')}{|\mathbf{r}-\mathbf{r}'|^3}dV'+\oint_{F'}\frac{(\mathbf{r}-\mathbf{r}')\mathbf{n}\cdot\mathbf{J}_s}{|\mathbf{r}-\mathbf{r}'|^3}dF'\right], \tag{11}$$

where $\mathbf{n}$ denotes the normal vector of the surface and F is the surface of the sample. Inserting this expression into Eq. (10) leads to a twofold volume integral which requires an impracticably high computational effort. A common approach to overcome this difficulty is the employment of Fourier transforms such as FFT to reduce the calculation onto local variables. The use of FFT demands a discretization on a regular grid. However, an essential feature of the calculation presented in this paper is the application of an adaptive mesh refinement technique yielding irregular positions of the nodal points which is required to obtain the necessary accuracy. Hence, another method for the evaluation of the stray field term is used.

1. Brown's upper bound

First, one may substitute $\mu_0\mathbf{H}_s=(\mathbf{B}-\mathbf{J}_s)$ in Eq. (10), where $\mathbf{B}$ is the magnetic induction. Instead of calculating $\mathbf{B}$ directly, one has the possibility to vary an arbitrary solenoidal field $\mathbf{B}'$ until it is approximately equal to $\mathbf{B}$. According to Brown[39,40] the functional

$$W(\mathbf{B}')=\frac{1}{2\mu_0}\int_{(\mathrm{all\ space})}(\mathbf{B}'-\mathbf{J}_s)^2 dV. \tag{12}$$

represents an upper bound for the stray field energy, where $\mathbf{B}'$ is an arbitrary solenoidal field. The minimum of the functional W is equal to the stray field energy, and is given if $\mathbf{B}'=\mathbf{B}$, i.e.,

$$E_{\mathrm{stray}}=W(\mathbf{B})\leqslant W(\mathbf{B}'). \tag{13}$$

This relation holds for any solenoidal field $\mathbf{B}'=\nabla\times\mathbf{A}$. Hence, minimizing W with respect to the (discretized) magnetic vector potential $\mathbf{A}$ yields the correct stray field energy and the corresponding magnetic induction. Introducing the new variables A_x, A_y, A_z at each nodal point, the functional W is calculated by means of the FEM. With this approximation $\mathbf{B}'$ is a piecewise constant function of the values $(\mathbf{A})_i$ at the nodes i. The kernel of the integral in Eq. (12) can be split up in three energy density contributions. With $\mathbf{B}'=\mathrm{const}$ within each element, the integration of $\mathbf{B}'^2/2\mu_0$ over an element is trivial. The same holds for the term $\mathbf{J}_s^2/2\mu_0$ which, by virtue of $|\mathbf{J}_s|=\mathrm{const}$ is spatially constant. The energy density from the mixed term $(-\mathbf{B}'\cdot\mathbf{J}_s/\mu_0)$ is interpolated linearly over the element in analogy to the anisotropy term.

2. Vector potential

The calculation of the demagnetizing field and the stray field energy by means of minimization of W yields a vector potential $\mathbf{A}$, discretized at each node. While the stray field and the stray field energy for a given distribution of magnetic moments is unique, the vector potential $\mathbf{A}$ is not. Only the solenoidal part of $\mathbf{A}$, from which the induction $\mathbf{B}=\nabla\times\mathbf{A}$ is derived, is unique for a given distribution of magnetic moments. The irrotational part of $\mathbf{A}$ does not have any physical meaning (gauge invariance). The numerically obtained discretized vector potential generally consists of both a solenoidal and an irrotational part. This vector potential is not gauged in order to allow for an unconstrained minimization of the functional W. The question may arise how the irrotational part of $\mathbf{A}$ is determined. As it is not used in the calculation of the energy, its value depends on the initial conditions and on the path the minimization routine takes on its way towards an energetic minimum. This imponderability of the resulting vector field may seem unsatisfactory. However, the relevant solenoidal part of $\mathbf{A}$ is not affected by the ambiguities of the calculated vector potential.

3. Exterior region

It has already been stressed that the integral in Eq. (12) is extended over the *whole* space. This ''open boundary'' problem is treated using spatial transforms for the external region[41] by means of which the unbounded exterior region is mapped on a finite area which is discretized and in which the calculation of the stray field is performed. By doing so, free boundary conditions for the vector potential are used. An efficient and seemingly more rigorous method to treat this open boundary problem is the use of boundary elements,[42] which we consider to implement in the algorithm in a future version. The method of integrating over both the magnetic region and the exterior region for the calculation of the demagnetizing field and its energy requires a high number of

elements and of unknowns. It is, however, by far more convenient than the direct evaluation of the integral in Eq. (10).

The calculation of the demagnetizing field used in our calculations is based on a program developed by Schrefl.[43]

E. Sum of all terms

Summing up all energy terms, we obtain the total energy of the system as a function of the set of variables ϑ_i, φ_i, and $(\mathbf{A})_i$. The equilibrium configuration of the magnetization is calculated by means of direct minimization with respect to these variables. For this purpose a commercial conjugate gradient method especially developed for large-scale problems is employed.[44]

Note that with this algorithm the spontaneous polarization $\mathbf{J}_s$ is defined only at the nodes. Only for visualization purposes it will be interpolated on a regular grid. In order to reduce computational time and cumulative discretization errors, the energy of the system is calculated in any case in the most direct way instead of interpolating the magnetization within the element and deriving the energy from it. This latter method has been used by Chen *et al.*[5] and is undoubtedly a useful assumption. However, the interpolation of the Cartesian components of $\mathbf{J}_s$ violates the constraint $|\mathbf{J}_s| = \text{const}$ and leads to higher computational costs for the second order terms, i.e., the anisotropy and the stray field, without necessarily yielding a higher accuracy.

F. Tests of the algorithm

We have performed several tests on the vector potential routine for different geometries. These tests consist in calculating the stray field energy for a fixed homogeneous magnetization. No influence of the initial configuration of $\mathbf{A}$ on the resulting energy and induction was found: Using a random initial vector potential yields the same results as a homogeneous one but requires longer computational time. The computed results for homogeneous magnetization parallel to the x, y, and z axis can be compared with analytical calculations of demagnetizing factors.[45] With increasing discretization density the theoretical values are generally approached very nicely.

The calculation of the demagnetizing field and its energy is most likely to be the source of possible errors in micromagnetic computations. Analytical proofs only exist for the case of homogeneously magnetized samples.[45] For the geometry used in the calculation presented here, the demagnetizing factors are[45] $N_x = 0.2939$, $N_y = 0.5629$, and $N_z = 0.1431$. The numerically obtained demagnetizing factors differ between 0.3% for N_x to 13% for N_z from the analytical values. We attribute this to the low discretization of the exterior region. Most of the elements are located in the magnetic region as flux closure patterns are expected. While for magnetization states with high remanence the accuracy of the calculation of the stray field in the exterior region is decisive, the stray field nearly vanishes outside the sample for flux closure structures and a comparatively low accuracy in the exterior region is sufficient in this case.

Recently we found that the vector potential method may lead to erroneous results concerning the stray field energy if the demagnetizing factors are very small. This is the case in thin platelets. The stray field energy is calculated in our case by means of the difference $\mathbf{B} - \mathbf{J}$. If $\mathbf{B}$ is essentially equal to $\mathbf{J}$, as is the case for demagnetizing factors close to zero, a very high accuracy is required in the calculation of $\mathbf{B}$ in order to obtain a correct value for the energy. The accuracy in the calculation of the magnetic structure, which is calculated by means of the coupling of $\mathbf{B}$ and $\mathbf{J}$, however, is not influenced by this effect.

The correctness of the anisotropy energy calculation can be tested easily by setting a homogeneous and fixed distribution of the magnetization enclosing different angles with the easy axis and comparing the result with the analytical value. Using a suitable inhomogeneous arrangement, the same can be done to test the exchange energy calculation. The exchange energy is influenced more sensitively by the discretization. However, these effects are reduced substantially by adaptive mesh refinement if the size of the discretization cells drops below the exchange length where the magnetization is strongly inhomogeneous.

VI. APPLICATION

With this algorithm the equilibrium distribution of the magnetization in a rectangular block of $Ni_{80}Fe_{20}$ ($A = 1.3 \times 10^{-11}$ J/m, $K = 500$ J/m^3, $J_s = 1.0$ T) is investigated. These material parameters yield $Q \simeq 10^{-3}$, i.e., a magnetically very soft material. The size and geometry of the sample is illustrated in Fig. 2.

The computational region is discretized into about 95 000 elements, approximately 83 000 of them are located inside the sample, the rest is used for the calculation of the demagnetizing field outside. The average extension of the elements within the sample is about 16 nm, the maximum distance found between two nodes of an element within the sample is 41 nm. Having the exchange length $\delta_N/\pi \simeq 6$ nm, this discretization is not expected to be sufficient to resolve the magnetic structure everywhere reliably. Therefore, an *a posteriori* adaptive mesh refinement technique is used to raise the accuracy of the calculation, see Sec. VII C.

VII. RESULTS

The starting conditions of the magnetization are chosen far from an equilibrium state in order to obtain demagnetized states that do not depend strongly on the initial configuration. Three homogeneous starting conditions (magnetization parallel to the x, y, and z axis) are used for the calculation. By doing so, two different patterns are obtained. The initialization parallel to the y axis yields the expected Landau pattern illustrated in Fig. 3.

In the other cases a seven-domain (''diamond'') pattern shown in Fig. 4 results. This diamond pattern has been reported, e.g., by Van Den Berg *et al.*[46] and represents a metastable state. The total energy of this configuration is in our case about 24% higher than the Landau pattern shown in Fig. 3.

The seven domain pattern and the Landau pattern have been found by Fredkin and Koehler[47,48] by means of *ab initio* micromagnetic calculations on Permalloy particles. The present paper focusses on the topology of the Landau structure which is supposed to be the energetical ground state of the system. The diamond pattern is analyzed elsewhere.[49]

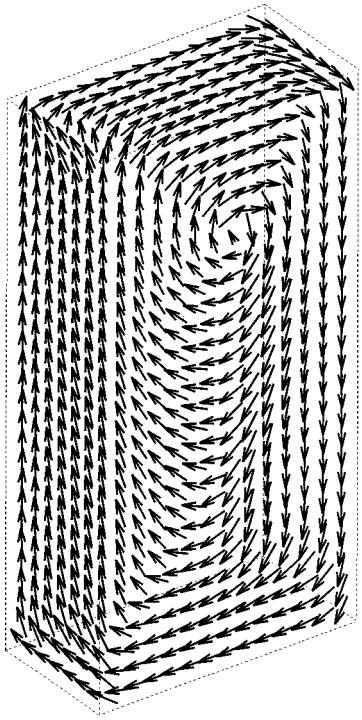

FIG. 3. 3D representation of the calculated Landau structure with four domains.

In addition to the clearly recognizable domain structure according to Fig. 1 some additional distinct features of the pattern in Fig. 3 can be found. First of all, the asymmetry of the magnetization at the surface with regard to an inversion at the center is evident. On the upper junction of the domain walls a magnetic vortex occurs while the lower junction is a

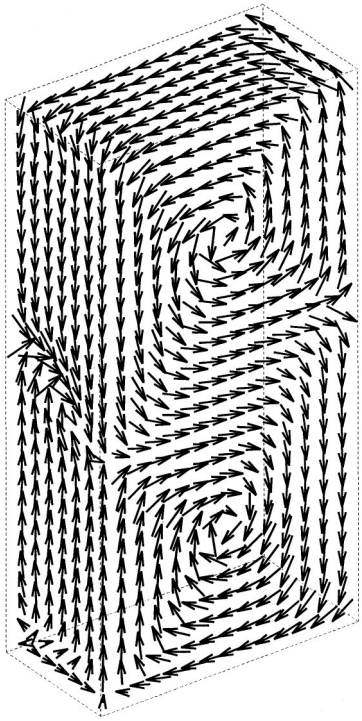

FIG. 4. 3D representation of the magnetization of the metastable seven-domain ''diamond'' structure.

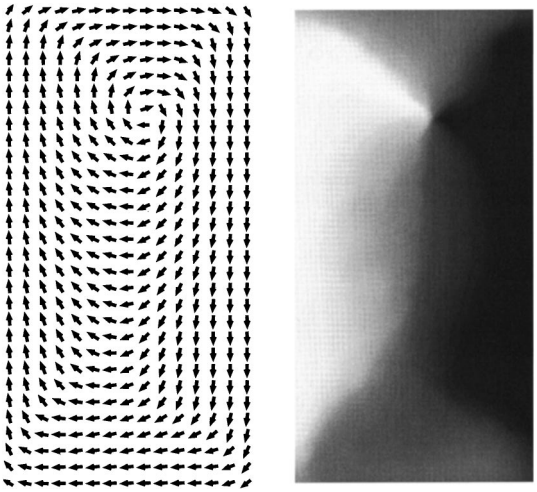

FIG. 5. Magnetization pattern at the surface of the Permalloy block (plane A in Fig. 8). Left: projection of the vector field on the surface. Right: Gray scale representation of the z component of the magnetization.

180° Néel wall. This effect resulting from the Néel walls at the surface has been discussed elsewhere.[19,34]

A. Canting of the central domain wall

Another striking peculiarity of the magnetization as compared with the idealized pattern in Fig. 1 is the asymmetrical shape of the closure domains shown in Fig. 5. The central domain wall appears to be canted with respect to the edge of the sample. The angle between one domain wall of the closure domain and the central domain wall is disparate for the two adjacent domain walls of the closure domain. The asymmetrical shape of the closure domains can be recognized clearly on the simulated Kerr image on the right side.

To analyze the magnetic structure more precisely we take a look at the magnetization inside the sample. The Figs. 6 and 7 show the projection of the magnetization on cross sections through the middle of the sample and on the rear side, respectively. The position of these cuts through the sample are described in Fig. 8. Remarkably, the asymmetry

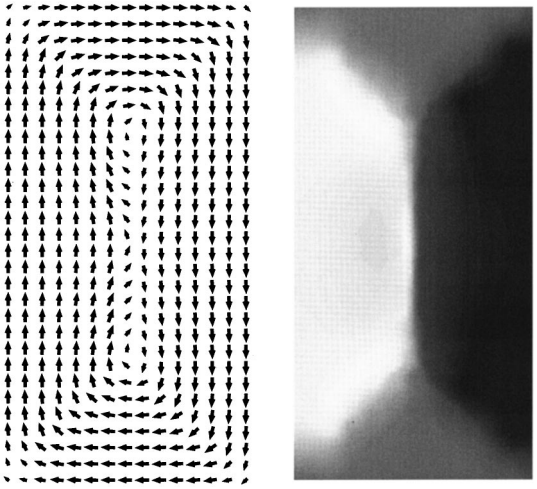

FIG. 6. Projection of the magnetization on the cross section B through the middle of the sample, see Fig. 8.

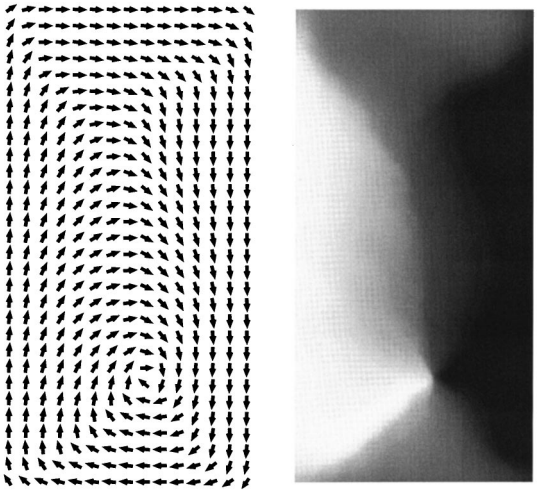

FIG. 7. Magnetization pattern on the rear side of the sample, plane C in Fig. 8.

of the domain pattern vanishes in the center of the sample (Fig. 6) while on the rear side the central domain wall is again skew, however, canted in the opposite direction compared with the front side shown in Fig. 5. Repetitions of the calculation have yielded different positions of the swirls and a canting of the central domain wall in both directions, i.e., left and right on the front side. These different results are assigned to slightly different starting conditions. In order to avoid the formation of metastable, unrealistic arrangements of high symmetry, a homogeneous starting condition is always perturbed randomly in our calculations prior to the minimization. The magnitude of this perturbation is typically about $\pm 0.5°$ for both ϑ_i and φ_i at each node i. The breaking of symmetry in different directions but in qualitatively equal manner indicates that this effect is not due to numerical artifacts or a consequence of the discrete numerical representation. As the patterns are basically the same and can be transformed into each other by means of simple symmetry operations, only one arrangement needs to be reported.

B. Bulk effects

To understand the reason for the skewness of the central domain wall it is helpful to study the topology of the magnetic domain walls. The magnetization on a cut through the middle of the sample across the plane $z=0$ (plane D in Fig. 8) is illustrated in Fig. 9. It shows that the transition between the two major magnetic domains is given by an asymmetrical Bloch wall. This wall type has been found independently by Hubert and LaBonte.[8,9] Using 2D calculations, the Hubert-LaBonte wall has been reported in other papers.[24,50] Our 3D modeling is in agreement with these results.

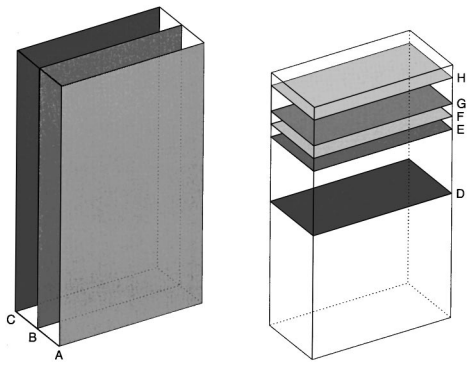

FIG. 8. Position of the cross sections shown in the subsequent figures. The locations of the planes are A: $y=125$ nm, B: $y=0$, C: $y=-125$ nm, D: $z=0$, E: $z=250$ nm, F: $z=300$ nm, G: $z=350$ nm, and H: $z=450$ nm. The viewpoint onto the cross-sections is located outside the sample on the positive y and z axes, respectively.

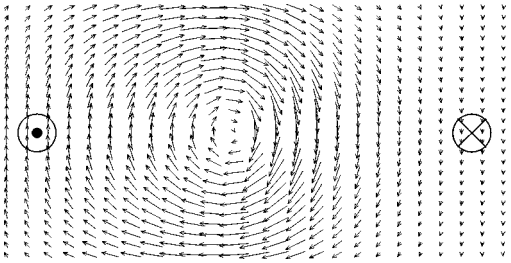

FIG. 9. Magnetization inside the sample on a cut through the plane $z=0$. The two major domains are separated by an asymmetrical Bloch wall (Hubert-LaBonte wall).

Symmetrical Bloch walls do not occur in magnetically soft material. A symmetrical Bloch wall, as illustrated schematically in Fig. 10, would lead to an out-of-plane magnetization at the surface. In soft magnetic materials such surface poles of the magnetization are avoided by the formation of so-called Néel caps, i.e., an alignment of the magnetic moments parallel to the surface. This behavior is known as Brown's pole avoidance principle.[51] Therefore, one has a mostly Néel-like transition between the domains on the surface while inside the sample the Bloch part of this domain wall prevails. As the Bloch wall at the center converts into a Néel wall near the surface, the magnetization is sheared on one side with respect to the center of the Bloch wall.[19,20] This shearing, in our case to the left side, can be seen in Fig. 9. On the other hand, the Néel-like magnetization on the lower side of Fig. 9 can be regarded as the far tail of the closure domain on the lower side of Fig. 5. Hence, the shearing of the magnetization near the surface gives rise to the asymmetrical shape of the closure domains.

The different cuts through the sample in Fig. 11 show how the magnetization inside evolves from the center to the upper end of the block in Fig. 3. The Hubert-LaBonte wall transforms continuously to a nearly homogeneous arrangement. The dashed circle in the cross section E shows the magnetization in the proximity of the swirl[52] (vortex) in Fig.

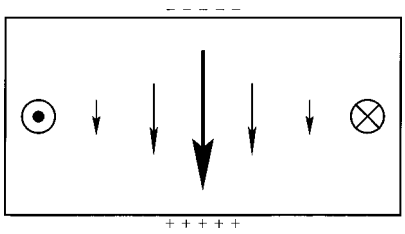

FIG. 10. Schematic representation of a symmetrical Bloch wall. As the Bloch wall intersects the surface of the sample, magnetic surface poles with high stray field energy occur. In soft magnetic material this is avoided by an alignment of the magnetic moments parallel to the surface, which leads to an asymmetrical Bloch wall as shown in Fig. 9.

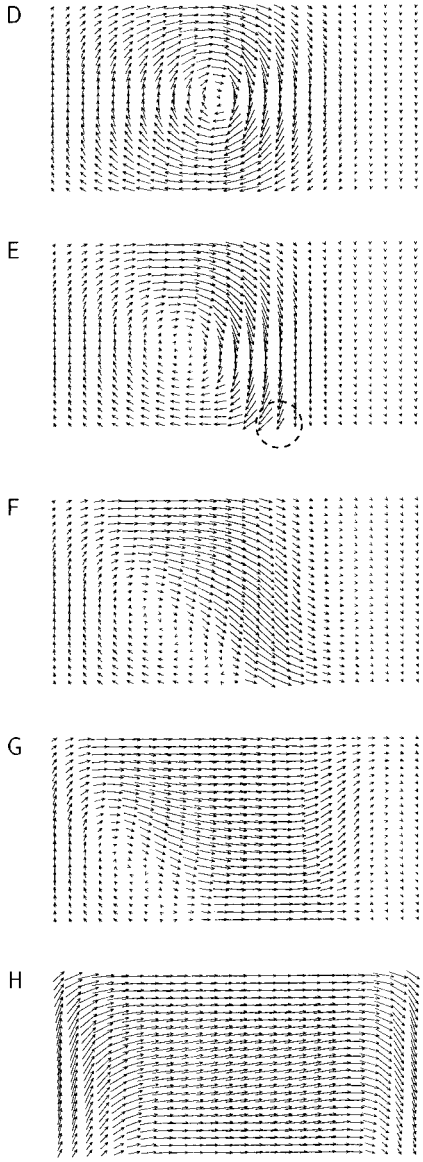

FIG. 11. Magnetization inside the sample on different planes with $z=\text{const}$ (see Fig. 8). The asymmetrical Bloch wall evolves continuously into a nearly homogeneous closure domain.

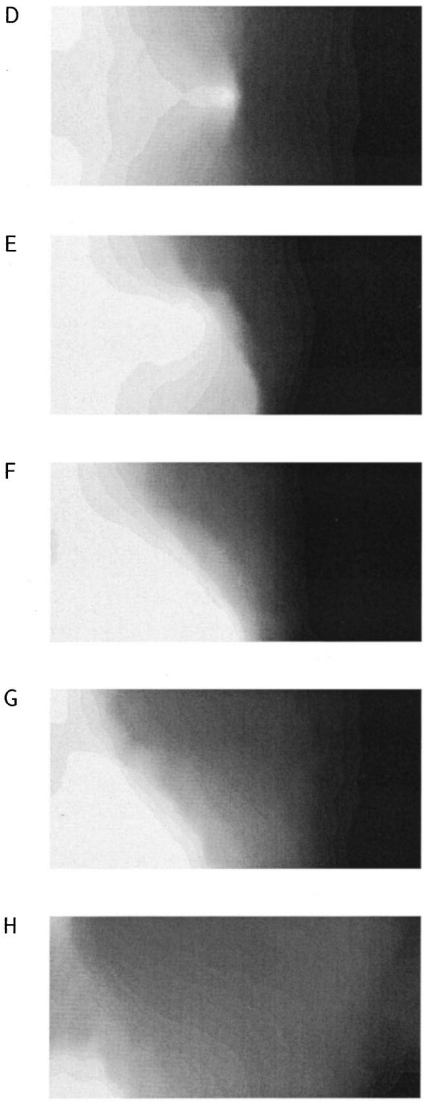

FIG. 12. Gray scale representation of the perpendicular component of the magnetization in the cross sections of Fig. 11.

5. Due to the asymmetry of the Hubert-LaBonte wall, the swirl is evidently displaced from the center of the sample. In the case of very thin layers, where the domains are separated by Néel walls, the closure domains have a symmetrical shape.[32,34] Hence, the asymmetry can be assigned to the Hubert-LaBonte wall.

The arrangement of the magnetization in the cross section F resembles to an asymmetrical Néel wall.[20] However, it should be stressed that rather than a transition from one type of 180° walls to another, the transition shown in Fig. 11 represents a series of cuts through different domains. A gray scale representation of the component of the magnetization perpendicular to these cuts is shown in the series of Fig. 12.

A corresponding series of cuts on the lower half of the block (not shown) yields in the same way a displaced swirl on the lower rear side of Fig. 3. Both vortices are displaced in the same direction $(-x)$. While the swirl on the upper side shows a perpendicular magnetization directed out of the sample, the perpendicular magnetization in the vortex core of the other swirl is oriented into the sample. This can be seen in the series of cross-sections along planes of $x=\text{const}$, cf. Fig. 13. The position of these cross sections is sketched in Fig. 14. In the cross section near the center of the sample [Fig. 13 (J)] the Bloch line[20,53] can be seen clearly, starting from one swirl in the lower left end ending in the other swirl on the upper right. The Bloch line is not located on a plane with $x=\text{const}$. The flux is carried from the lower swirl which is displaced from the center in negative direction of x over to the line sketched in Fig. 13 (J) (at $x>0$) towards the upper swirl, which is again displaced towards negative values of x. Figures 13 (I) and 13 (K) show how the magnetization tends to align parallel to the edges of the sample in order to avoid surface poles. This leads to different configurations of the magnetization in the eight corners of the sample.[52] Several different combinations of arrangements in the corners are possible, but the analysis of these details lies outside the scope of this paper.

Despite the formation of Néel caps the perpendicular component of the magnetization does not vanish completely at the surface. As illustrated in Fig. 15 the perpendicular

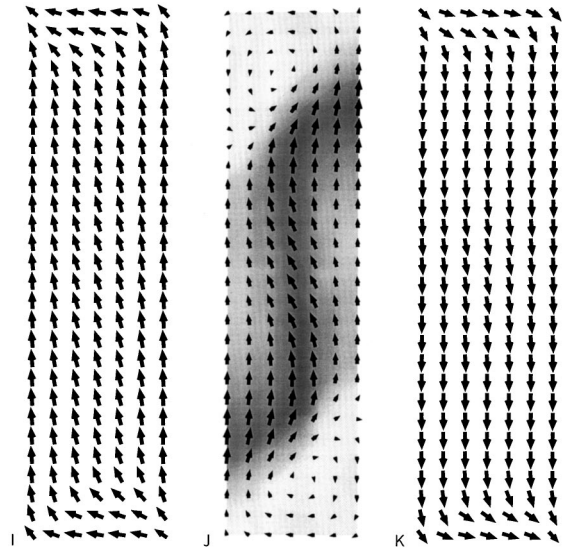

FIG. 13. Magnetization on the planes $x=\text{const}$ shown in Fig. 14. The approximate position of the Bloch line is the gray shaded area in J, which indicates the region where m_x is close to zero. The gray scaling represents the value of m_x^2.

component shows a characteristic pattern at the surface. However, except for the swirl and the corners, the magnitude of this out-of-plane magnetization is very small (about 10% of J_s).

C. Effect of the mesh refinement

It has been mentioned previously that an adaptive meshing method has been used for the calculation. As the visualization of a three-dimensional grid of irregular tetrahedral elements is problematic, only the mesh at the surface of the sample is displayed in Fig. 16.

The adaptive mesh refinement is performed in a first step increasing the discretization density in areas of inhomogeneous magnetization by means of the ''shrinking element'' technique.[31] This method is a *r*-type refinement method which essentially shifts the nodal points towards inhomogeneous regions. As can be seen in Fig. 16 the nodal point density is higher where the domain walls are located. How-

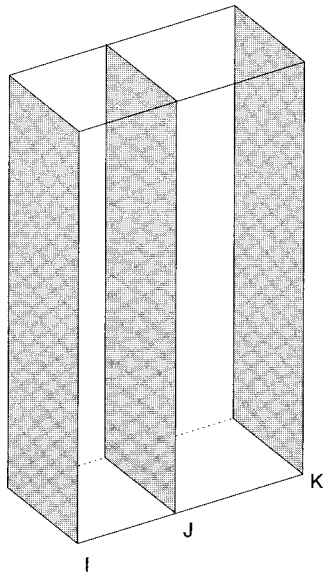

FIG. 14. Position of the cross sections in Fig. 13. The cross section J is located at $x=25$ nm. The planes are viewed at from the positive x axis.

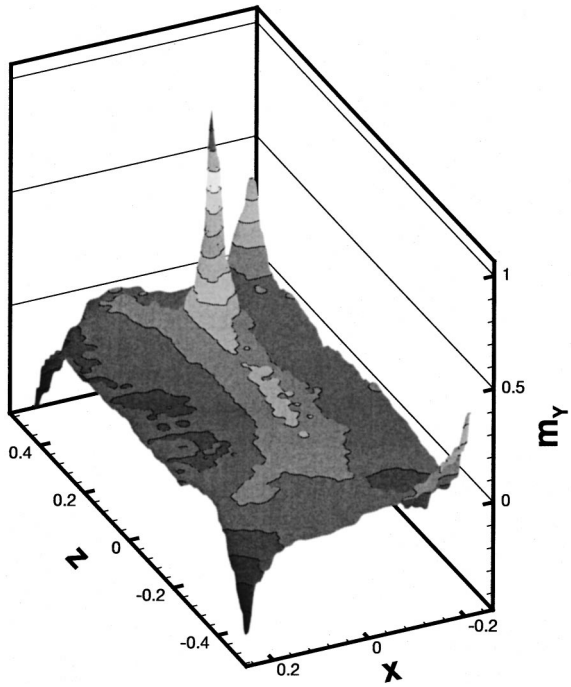

FIG. 15. Topology of the perpendicular component at the surface. The peak represents the out-of-plane magnetization at the core of the swirl. At the corners the magnetization turns towards the adjacent edges [cf. Figs. 13 (I), 13 (K), 11 (H)] and the perpendicular component increases. A small Bloch-like contribution to the central Néel wall at the surface can be recognized in the middle.

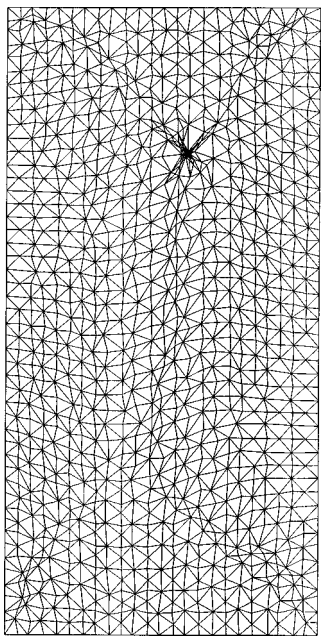

FIG. 16. Refined mesh on the surface of the sample. The adapted mesh has been generated using the ''shrinking element'' technique combined with a *h*-type refinement.[31] The regions of stronger inhomogeneities of the magnetization are recognized, see Fig. 5. In these areas the density of nodal points is increased.

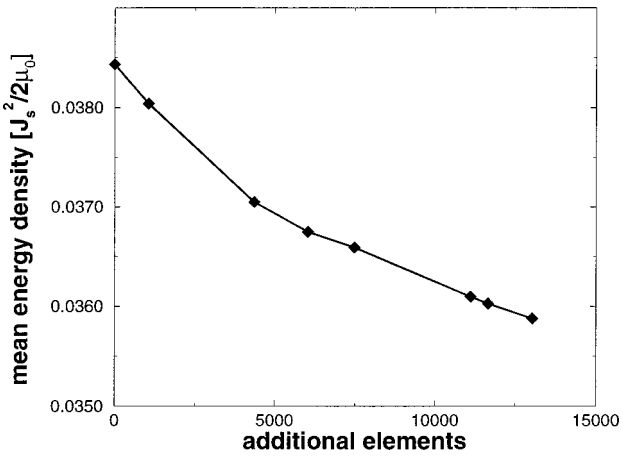

FIG. 17. Changement of the mean energy density with increasing mesh refinement. The total energy of the arrangement diminishes slightly with increasing discretization density. The mean energy density is expressed in reduced units, i.e., in units of $J_s^2/2\mu_0$.

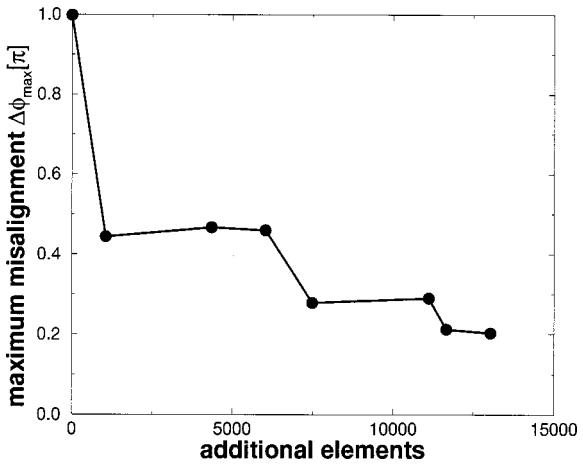

FIG. 19. The maximum misalignment of magnetic moments in the finite elements can be associated with the maximum error of the calculation. This misalignment $\Delta\varphi_{\max}$ is reduced strongly by means of the adaptive mesh refinement.

ever, moving nodal points is not sufficient to resolve strongly inhomogeneous regions such as a magnetic swirl because a big displacement of nodal points is likely to yield a strongly distorted mesh with ill-shaped elements. Therefore, another refinement strategy is employed in a second step. By means of bisection of elements, nodal points are added specifically in strongly inhomogeneous regions. This mesh refinement algorithm recognizes the insufficient discretization in the swirl and adds new nodal points in this area. Iteratively, the mesh is modified and a new minimum energy arrangement is calculated. The effect of this procedure on the total energy is illustrated in Fig. 17. While the total energy decreases with higher discretization density, the exchange energy rises, see Fig. 18. A coarse discretization mesh tends to underestimate the exchange energy and leads to an overestimation of the stray field energy in this algorithm. In the mesh with the highest number of elements, the maximum edge length of the elements within the refined region becomes small, between 0.5 and 1.0 nm which is significantly below the exchange length.

Although after the refinement the magnetization does not change visibly, the error of the calculation is reduced significantly. In numerical micromagnetic calculations, discretization errors occur in the case that the magnetization at neighboring discretization points is strongly misaligned. Correspondingly, the maximum misalignment of the magnetization in an element of the mesh can be used as an indicator for the quality of the mesh. The maximum misalignment of magnetic moments in adjacent nodal points is lowered effectively by means of the adaptive mesh refinement as illustrated in Fig. 19.

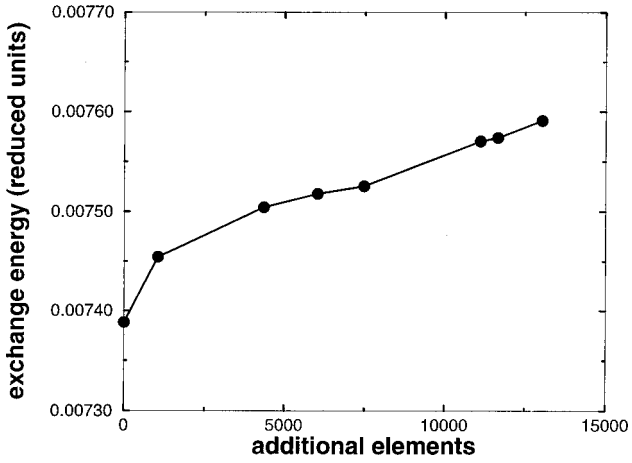

FIG. 18. Mean exchange energy density expressed in reduced units versus number of additional elements.

VIII. COMPARISON WITH WALL MODEL CALCULATION

The total energy resulting from the numerical calculation can be compared with a simplified analytical wall model calculation using a method described in detail by Aharoni.[18] According to this, the width Δ_B of a one-dimensional 180° Bloch wall in an infinite film with thickness d obeys the equation

$$\frac{A}{\Delta_B^2}(\sqrt{2}-1)=\frac{K_1}{2}+\frac{J_s^2}{2\mu_0}\left[\frac{2\Delta_B}{d}\ln\left(1+\frac{d}{2\Delta_B}\right)-\frac{\Delta_B}{2\Delta_B+d}\right]. \tag{14}$$

Similarly, the Néel wall width Δ_N can be determined from the equation

$$\frac{A}{\Delta_N^2}(\sqrt{2}-1)=\frac{K_1}{2}+\frac{J_s^2}{2\mu_0}\left[\frac{1}{2}-\frac{2\Delta_N}{d}\ln\left(1+\frac{d}{2\Delta_N}\right)+\frac{\Delta_N}{2\Delta_N+d}\right]. \tag{15}$$

The energy per unit wall area $\gamma^{180°}$ is calculated according to

$$\gamma_B^{180°}=\frac{\pi A}{\Delta_B}(\sqrt{2}-1)+\frac{\pi\Delta_B K_1}{2}+\frac{\pi J_s^2}{2\mu_0}\frac{\Delta_B^2}{d}\ln\left(1+\frac{d}{2\Delta_B}\right) \tag{16}$$

for the Bloch wall and

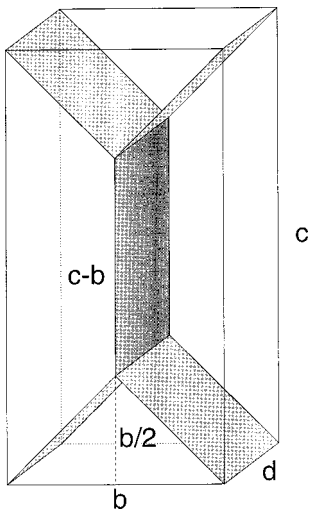

FIG. 20. Idealized wall structure used in the analytical calculation. The length of the edges are $b=500\,\mathrm{nm}$, $c=1\,\mu\mathrm{m}$, and $d=250\,\mathrm{nm}$.

$$\gamma_N^{180^\circ}=\frac{\pi A}{\Delta_N}(\sqrt{2}-1)+\frac{\pi\Delta_N K_1}{2}++\frac{\pi J_s^2\Delta_N}{4\mu_0}\times\left[1-\frac{2\Delta_N}{d}\ln\left(1+\frac{d}{2\Delta_N}\right)\right] \tag{17}$$

for the Néel wall. The material parameters J_s, K_1, and A for Permalloy given in Sec. VI are used, the thickness d is 250 nm. Solving numerically the transcendental equations (14) and (15) yields $\Delta_B=9.12\,\mathrm{nm}$ and $\Delta_N=6.00\,\mathrm{nm}$. With these values one obtains from Eqs. (16) and (17) $\gamma_B^{180^\circ}=2.98\times10^{-3}\,\mathrm{J/m^2}$ and $\gamma_N^{180^\circ}=6.02\times10^{-3}\,\mathrm{J/m^2}$. For 90° Néel walls we approximate

$$\gamma_N^{90^\circ}\simeq\frac{1}{2}\gamma_N^{180^\circ}. \tag{18}$$

As a simplified model for the Landau structure of the magnetization we consider a geometry of the domain wall structure sketched in Fig. 20. Assuming 90° Néel walls at the borders of the closure domains and a 180° Bloch wall as the central domain wall the total energy Φ_{tot} writes

$$\Phi_{\mathrm{tot}}=d\left[(c-b)\gamma_B^{180^\circ}+b\gamma_N^{90^\circ}2\sqrt{2}+\frac{1}{2}b^2K_1\right] \tag{19}$$

$$\simeq 0.0292\frac{J_s^2}{2\mu_0}bcd. \tag{20}$$

The last term in Eq. (19) accounts for the magnetization perpendicular to the easy axis in the closure domains. The value of 0.0292 of the reduced mean energy density is of the same order of magnitude as the computed result, see Fig. 17. However, the result from the analytical calculation differs by about 22% from the numerical result. This difference can be attributed to several simplifications used in the wall model calculation. For instance, finite-size effects such as surface charges at the corners and the complex structure of the magnetization in the vicinity of the swirls are neglected in the analytical model. Moreover, the energy per unit wall area $\gamma_{B,N}^{180^\circ}$ and the domain wall widths $\Delta_{B,N}$ are calculated assuming an infinitely extended thin film, which is only a coarse approximation in this case. If we assume that the central domain wall consists in equal parts of both a Néel- and a Bloch-like component [Fig. 11 (D)], we may set $\gamma^{180^\circ}=(\gamma_B^{180^\circ}+\gamma_N^{180^\circ})/2$ and thus obtain $\Phi_{\mathrm{tot}}\simeq 0.033bcdJ_s^2/2\mu_0$, which corresponds rather nicely to the calculated value. This agreement should not be interpreted as a proof of the result because of the simplifications involved in the analytical calculation. However, considering that the computed arrangement of magnetic moments in the Landau structure is strongly inhomogeneous over nearly the whole sample and that the idealized structure sketched in Fig. 20 hardly describes the actual arrangement of the magnetization, the comparison of the computed result with this simple wall model calculation yields reasonable agreement. It is expected to obtain a better agreement with analytical model calculations for samples of bigger size, which however are currently precluded from numerical micromagnetic investigations due to the high computational requirements.

IX. COMPARISON WITH EXPERIMENTAL DATA

The most unexpected result of the presented calculation is the asymmetrical shape of the closure domains at the surface of the sample. A report on this effect has not been found in the literature.

An experimental detection of the forecasted asymmetrical domain structure is expected to be problematic for different reasons. First, it should be kept in mind that the effect is very small though the canting of the central domain wall of about 7° shown in Figs. 5 and 7 is clearly visible: The specimen used in experimental domain wall observations are usually significantly larger than the sample considered in this calculation. The displacement of the junction of the domains with respect to the center, which leads to the asymmetrical shape, is in this calculation about 40 nm. This effect is due to the asymmetrical structure of the Bloch wall which is expected to depend only on the thickness of the film and not on the finite size of a platelet. Provided that the core of the magnetic vortex is shifted in a region within the width of the central domain wall the inclination angle of the domain wall at the surface depends only on the distance of the two swirls. As the characteristic size of the films observed in experiments is typically of about 100 μm, such a small displacement would lead to a very small tilting angle. Hence, the strong canting in our calculation must be attributed to the small size of the sample.

The asymmetry of the arrangement occurs only on the surfaces, and on the front side it is opposed to the asymmetry on the rear side. If a domain structure is investigated by means of transmission methods such as the Lorentz microscopy the deflection pattern generally represents an integral over the thickness of the film. Hence, the asymmetry on the surfaces is expected to be averaged out in a Lorentz microscopy image. The displacement on opposite sides on the front and on the rear would merely lead to a smearing out of the domain wall image. Nevertheless, there seems to be a qualitative agreement with the structure predicted from our calculation and experimental observation reported in the literature. In thick soft magnetic films, magnetic domain walls are usu-

ally separated by the typical double-Y domain wall structure. A careful observation of the domain patterns reported by Tsukahara[54] and Kawakatsu[55,56] or, e.g., by Harrison and Leaver[57] suggests that a plane parallel to the film normal through the middle of the central domain wall is not a plane of symmetry. The 90° walls on opposite sides of the double-Y structure are parallel, respectively, but neighboring 90° walls seem to enclose a different angle with the central domain wall. Magneto-optical Kerr spectroscopy observations[58] of the domain structure in iron films suggest a slight tilting of the central domain wall.

X. CONCLUSION

The computation of the Landau structure in a soft magnetic flat rectangular prism has provided a possible solution of a well-known and formerly unsolved problem in micromagnetics. The obtained result indicates that the idealized Landau structure represents a rather coarse model of the actual distribution of the magnetic moments inside the sample. Even in this most simple magnetic domain pattern in a bulk soft magnetic sample the topology of the magnetization is remarkably complex. Nevertheless, the computed total energy of the system is comparable to the result of an analytical calculation using a strongly simplified wall model. Bulk effects enfavor the formation of domain structures of lower symmetry compared with the domain structure in thin films. The asymmetry of the central Bloch wall gives rise to a distorted shape of the magnetic domains. Experimental observations suggest that the magnetic structure is qualitatively transferable to soft magnetic samples of considerably larger size than the geometry used in this calculation.

[1] W. F. Brown, Jr., Phys. Rev. **58**, 736 (1940).
[2] W. F. Brown, Jr., Phys. Rev. **60**, 139 (1941).
[3] W. F. Brown, Jr., *Micromagnetics* (Interscience, New York, 1963).
[4] M. E. Schabes and H. N. Bertram, J. Appl. Phys. **64**, 1347 (1988).
[5] W. Chen, D. R. Fredkin, and T. R. Koehler, IEEE Trans. Magn. **29**, 2124 (1993).
[6] T. Schrefl, H. Kronmüller, and J. Fidler, Phys. Rev. B **49**, 6100 (1994).
[7] R. Fischer and H. Kronmüller, Phys. Rev. B **54**, 7284 (1996).
[8] A. Hubert, Phys. Status Solidi **32**, 519 (1969).
[9] A. E. LaBonte, J. Appl. Phys. **40**, 2450 (1969).
[10] W. F. Brown, Jr. and A. E. La Bonte, J. Appl. Phys. **36**, 1380 (1963).
[11] Round-robin results for a $2\,\mu\text{m}\times1\,\mu\text{m}\times20\,\text{nm}$ Permalloy platelet are available at http://cobalt.nist.gov/mumag/prob1/prob1report.html
[12] T. L. Gilbert, Phys. Rev. **100**, 1243 (1955).
[13] A. Aharoni, J. Appl. Phys. **51**, 5906 (1980).
[14] A. Aharoni, J. Appl. Phys. **63**, 5879 (1988); **64**, 3330(E) (1988).
[15] W. Rave, K. Fabian, and A. Hubert, J. Magn. Magn. Mater. **190**, 332 (1998).
[16] L. Landau and E. M. Lifshitz, Phys. Z. Sowjetunion **8**, 153 (1935).
[17] R. V. Coleman and G. G. Scott, Phys. Rev. **107**, 1276 (1957).
[18] A. Aharoni, *Introduction to the Theory of Ferromagnetism* (Clarendon, Oxford, 1996).
[19] A. S. Arrott and T. L. Templeton, Physica B **233**, 259 (1997).
[20] A. Hubert, *Theorie der Domänenwände in Geordneten Medien*, Lecture Notes in Physics (Springer, Berlin, 1974).
[21] E. Feldtkeller, Z. Angew. Phys. **19**, 530 (1965).
[22] F. Bloch, Z. Phys. **74**, 295 (1932).
[23] L. Néel, C. R. Hebd. Seances Acad. Sci. **241**, 533 (1955).
[24] K. Ramstöck, W. Hartung, and A. Hubert, Phys. Status Solidi A **155**, 505 (1996).
[25] T. R. Koehler and D. R. Fredkin, IEEE Trans. Magn. **27**, 4763 (1991).
[26] H. Kronmüller, Z. Phys. **168**, 478 (1962).
[27] S. Middelhoek, J. Appl. Phys. **34**, 1054 (1963).
[28] R. W. Chantrell, K. M. Tako, M. Wongsam, N. Walmsley, and T. Schrefl, J. Magn. Magn. Mater. **175**, 137 (1997).
[29] S. McFee, IEEE Trans. Magn. **33**, 4116 (1997).
[30] D. Lewis and E. Della Torre, IEEE Trans. Magn. **33**, 4161 (1997).
[31] R. Hertel and H. Kronmüller, IEEE Trans. Magn. **34**, 3922 (1998).
[32] S. Huo, J. E. L. Bishop, J. W. Tucker, W. M. Rainforth, and H. A. Davies, IEEE Trans. Magn. **33**, 4170 (1997).
[33] N. Hayashi, T. Inoue, Y. Nakatani, and Y. Uesaka, IEEE Trans. Magn. **24**, 3111 (1988).
[34] H. Kronmüller, R. Fischer, R. Hertel, and T. Leineweber, J. Magn. Magn. Mater. **175**, 177 (1997).
[35] B. Joe, Adv. Eng. Softw. **13**, 325 (1991).
[36] M. C. Rivara, SIAM (Soc. Ind. Appl. Math.) J. Numer. Anal. **21**, 604 (1984).
[37] P. P. Silvester and P. L. Ferrari, *Finite Elements for Electrical Engineers* (Cambridge University Press, Cambridge 1996).
[38] N. Kikuchi, *Finite Element Methods in Mechanics* (Cambridge University Press, Cambridge, 1986).
[39] W. F. Brown, Jr., J. Phys. Soc. Jpn. **17**, 540 (1962).
[40] A. Aharoni, IEEE Trans. Magn. **27**, 4793 (1991).
[41] X. Brunotte, G. Meunier, and J. F. Imhoff, IEEE Trans. Magn. **28**, 1663 (1992).
[42] B. Yang and D. R. Fredkin, IEEE Trans. Magn. **34**, 3842 (1998).
[43] T. Schrefl, J. Fidler, and H. Kronmüller, J. Magn. Magn. Mater. **138**, 15 (1994).
[44] P. E. Gill, W. Murray, and M. H. Wright, *Practical Optimization* (Academic, London, 1981).
[45] A. Aharoni, J. Appl. Phys. **83**, 3432 (1998).
[46] H. A. M. Van Den Berg and D. K. Vatvani, IEEE Trans. Magn. **18**, 880 (1982).
[47] D. R. Fredkin and T. R. Koehler, J. Appl. Phys. **67**, 5544 (1990).
[48] D. R. Fredkin and T. R. Koehler, IEEE Trans. Magn. **26**, 1518 (1990).
[49] R. Hertel and H. Kronmüller, J. Appl. Phys. **85**, 6190 (1999).
[50] M. R. Scheinfein, J. Unguris, J. L. Blue, K. J. Caokley, D. T. Pierce, R. J. Celotta, and P. Ryan, Phys. Rev. B **43**, 3395 (1991).
[51] W. F. Brown, Jr., *Magnetostatic Principles in Ferromagnetism* (North-Holland, Amsterdam, 1962).
[52] A. Hubert, J. Phys. (France) **49**, 1859 (1988).
[53] J. Miltat and P. Trouilloud, J. Phys. (France) **49**, 1947 (1988).

[54] S. Tsukahara, IEEE Trans. Magn. **20**, 1876 (1984).
[55] S. Tsukahara and H. Kawakatsu, J. Phys. Soc. Jpn. **32**, 72 (1972).
[56] S. Tsukahara and H. Kawakatsu, J. Phys. Soc. Jpn. **32**, 1493 (1972).
[57] C. G. Harrison and K. D. Leaver, Phys. Status Solidi A **15**, 415 (1973).
[58] A. Hubert, *Kerroptische Mikroskopie* (VFA, Jülich, 1993), Vol. 24.